Journal of Cranio-Maxillo-Facial Surgery 52 (2024) 127–135

Contents lists available at ScienceDirect

Journal of Cranio-Maxillo-Facial Surgery

journal homepage: www.jcmfs.com

Bone regeneration in critical-size defects of the mandible using biomechanically adapted CAD/CAM hybrid scaffolds: An in vivo study in miniature pigs

Juliane Wagner [a,b,*], Sascha Luck [a], Klaas Loger [a], Yahya Açil [a], Johannes H. Spille [a], Sascha Kurz [c], Matthias Ahlhelm [d], Eric Schwarzer-Fischer [d], Lena-Christin Ingwersen [e], Anika Jonitz-Heincke [e], Sam Sedaghat [f], Jörg Wiltfang [a], Hendrik Naujokat [a]

[a] Department of Oral and Maxillofacial Surgery, University Hospital Schleswig-Holstein, Campus Kiel, Kiel, Germany
[b] Cluster of Excellence, Precision Medicine in Inflammation, Christian-Albrechts-University of Kiel, Kiel, Germany
[c] ZESBO — Center for Research on Musculoskeletal Systems, Leipzig University, Leipzig, Germany
[d] Fraunhofer Institute for Ceramic Technologies and Systems, IKTS, Dresden, Germany
[e] Biomechanics and Implant Technology Research Laboratory, Department of Orthopaedics, Rostock University Medical Center, Rostock, Germany
[f] Department of Diagnostic and Interventional Radiology, University Hospital Heidelberg, Heidelberg, Germany

ARTICLE INFO

Handling Editor: Prof. Emeka Nkenke

ABSTRACT

The study aimed to analyze bone regeneration in critical-size defects using hybrid scaffolds biomechanically adapted to the specific defect and adding the growth factor *rh*BMP-2.

For this animal study, ten minipigs underwent bilateral defects in the corpus mandibulae and were subsequently treated with novel cylindrical hybrid scaffolds. These scaffolds were designed digitally to suit the biomechanical requirements of the mandibular defect, utilizing finite element analysis. The scaffolds comprised zirconium dioxide-tricalcium phosphate (ZrO_2-TCP) support struts and TCP foam ceramics. One scaffold in each animal was loaded with *rh*BMP-2 (100 µg/cm^3), while the other served as an unloaded negative control. Fluorescent dyes were administered every 2 weeks, and computed tomography (CT) scans were conducted every 4 weeks. Euthanasia was performed after 3 months, and samples were collected for examination using micro-CT and histological evaluation of both hard and soft tissue.

Intravital CT examinations revealed minor changes in radiographic density from 4 to 12 weeks postoperatively. In the group treated with *rh*BMP-2, radiographic density shifted from 2513 ± 128 (mean ± SD) to 2606 ± 115 Hounsfield units (HU), while the group without *rh*BMP-2 showed a change from 2430 ± 131 to 2601 ± 67 HU. Prior to implantation, the radiological density of samples measured 1508 ± 30 mg HA/cm^3, whereas post-mortem densities were 1346 ± 71 mg HA/cm^3 in the *rh*BMP-2 group and 1282 ± 91 mg HA/cm^3 in the control group ($p = 0.045$), as indicated by micro-CT measurements. The histological assessment demonstrated successful ossification in all specimens. The newly formed bone area proportion was significantly greater in the *rh*BMP-2 group (48 ± 10%) compared with the control group without *rh*BMP-2 (42 ± 9%, $p = 0.03$). The mean area proportion of remaining TCP foam was 23 ± 8% with *rh*BMP-2 and 24 ± 10% without *rh*BMP-2.

Successful bone regeneration was accomplished by implanting hybrid scaffolds into critical-size mandibular defects. Loading these scaffolds with *rh*BMP-2 led to enhanced bone regeneration and a uniform distribution of new bone formation within the hybrid scaffolds. Further studies are required to determine the adaptability of hybrid scaffolds for larger and potentially segmental defects in the maxillofacial region.

* Corresponding author. Department of Oral and Maxillofacial Surgery, University Hospital Schleswig-Holstein, Campus Kiel, Arnold-Heller-Straße 3, Kiel, Germany

E-mail address: juliane.wagner@uksh.de (J. Wagner).

https://doi.org/10.1016/j.jcms.2023.11.007
Received 7 September 2023; Accepted 23 November 2023
Available online 29 November 2023

1. Introduction

Treating and rehabilitating critical-size bone defects within the maxillofacial region presents significant challenges for patients and practitioners. Presently, the primary approach involves utilizing autologous bone grafts. Depending on the specifics of the defect, microvascular pedicled fibula, scapula, or iliac crest grafts are the primary choices (Wang et al., 2011). However, the mechanical characteristics of allogeneic, xenogeneic, or alloplastic bone graft substitutes still lack the necessary suitability for clinical application in cases involving extensive defects.

It is widely acknowledged that complications frequently arise during this process, encompassing issues such as graft misfit and complications tied to the donor site (Feuvrier et al., 2016; Zimmermann et al., 2001). Morbidities manifest not only immediately following the surgical procedure, which poses risks due to the duration of the operation and anticipated blood loss, but also during the recovery period. Severe complications can occur, including infections and thromboses of the donor site extremities, and the development of compartment syndrome (Berzofsky et al., 2013).

In recent years, the digital planning of patient-specific saw-cut templates, drill guides, and osteosynthesis plates has gained significant traction in clinical practice. While this advancement greatly enhances the reconstruction of craniofacial defects, the issue of donor site morbidity persists. Furthermore, the predefined shape of the graft often proves challenging to seamlessly conform to the three-dimensional anatomy of the recipient site (Ganry et al., 2017; Rana, 2017; Rana et al., 2017; Ritschl et al., 2017).

Alloplastic materials, such as titanium, ceramics, or plastic implants, can offer utility in appropriate cases, such as bridging segment defects (Jo et al., 2018; Khorasani et al., 2018; Patel and Brandstetter, 2016). These facilitate the achievement of a well-fitting shape and contribute to minimizing surgical morbidity. However, a central issue persists: these materials lack biological activity and serve solely as placeholders, devoid of the capacity for bone regeneration. The mechanical instability inherent in these materials can lead to complications, including infections and bone resorption (Sadr-Eshkevari et al., 2013), particularly accentuated within the already challenging contexts of pre-operated patients or instances such as pre-existing osteomyelitis.

In principle, allogeneic and xenogeneic bone replacement materials, which gradually give way to the patient's bone, offer an exceptional means to maintain stable and irritation-free conditions (Gruskin et al., 2012). However, their application is restricted to small defects due to inherent mechanical instability (Yamada and Egusa, 2018). Within the factor-β family of growth factors, bone morphogenetic proteins (BMPs) play a vital role in bone regeneration and drive *de novo* bone formation (Kirker-Head, 2000; Wang et al., 1988; Wozney et al., 1988; Yamaguchi et al., 1996). Of these proteins, BMP-2 is the most extensively studied. It is recognized for its capacity to stimulate cell proliferation, differentiation, and chemotaxis (Sampath et al., 1992; Yamashita et al., 1996). The distribution form of BMP-2 is known as *rh*BMP-2.

To enhance primary stability, framework materials can be employed. Essentially, the ideal biotechnological bone replacement is mechanically robust and capable of conforming to the unique contours of an individual defect. Its microstructure fosters osteoconduction, facilitating bone cell attachment and bone extracellular matrix synthesis, and supporting tissue vascularization. Moreover, osteoinductive growth factors can further bolster cell growth (Becker et al., 2009; Miron and Zhang, 2012; Moore et al., 2001). Our study aimed to assess in vivo bone regeneration within critical-size mandibular defects in miniature pigs, utilizing newly developed hybrid scaffolds. A key advancement in these hybrid scaffolds is their tailored mechanical properties to suit the specific demands of defects, coupled with a hybrid design encompassing supportive struts and a degradable osteoconductive matrix.

2. Materials and methods

2.1. Experimental animals

The study comprised ten fully grown female miniature pigs (Ellegaard Göttingen Minipigs) with an average weight of 40.7 kg (range: 33–49 kg). Because of their bone metabolism characteristics, which are similar to those of humans, miniature pigs are highly appropriate for bone implant studies. The study received approval from the Ministerium für Energiewende, Landwirtschaft, Umwelt, Natur und Digitalisierung Schleswig-Holstein (ref: AZ: V242-75139/2020(100-11/20)).

2.2. Hybrid bone scaffolds

A load-bearing support structure was additively manufactured for the hybrid bone implant using the CerAM VPP (vat photopolymerization) method. This pressure-loadable support structure was constructed from a composite material of zirconium dioxide-tricalcium phosphate (ZrO_2-TCP) in a 60:40 vol% ratio. The framework incorporated holes for screw fixation. The support structure was filled and enveloped with a porous ceramic, so-called freeze foam, made of TCP using the freeze-foaming technique (Ahlhelm et al., 2016, 2017, 2021).

The cylindrical scaffolds, measuring approximately 14 × 12 mm, were designed using computer-aided techniques (Fig. 1A) in a truss–column hybrid configuration (SolidWorks, 2021; Dassault Systèmes SE, Vélizy-Villacoublay, France). These designs were then subjected to analysis and iterative optimization using the finite element method (ANSYS Workbench 17.1; ANSYS, Inc., Canonsburg, PA, USA).

The CerAM VPP method was used to creat the load-bearing support structure during the initial fabrication stage. This involved preparing a bioceramic suspension using calcined hydroxyapatite (HAp; sourced from Merck KGaA, Darmstadt, Germany; BET = 70.01 m^2/g, d50 = 2.64 μm) and zirconia (TZ-3Y-E, TOSOH, d50 = 0.73 μm). The pressure-loadable support structures were produced using the CeraFab 7500 printing device (Lithoz GmbH, Vienna, Austria). After the 3D printing process, the green samples underwent cleaning, debinding up to 600 °C (in a nitrogen atmosphere), and presintering up to 1000 °C (in an air atmosphere). The support frame had holes for screw fixation (Fig. 1B).

In the second stage of fabrication, a suspension of HAp was prepared. This HAp suspension and the previously manufactured support structure were snugly placed within a dedicated cylindrical rubber mould. This mould maintained the scaffold's intended cylindrical shape throughout the freeze-foaming process. Following freeze-foaming, the hybrid scaffolds underwent sintering at a temperature of 1250 K for 1.5 h (Fig. 1C). The composite freeze foams exhibited a porosity ranging from 60 to 70%. The compressive strength of these hybrid scaffolds was determined as 5.7 ± 0.8 MPa through testing conducted with Allroundline Z10 apparatus (Zwick/Roell GmbH & Co. KG, Ulm, DE).

2.3. Scaffold preparation

All scaffolds underwent a heat sterilization process at 180 °C for 3 h. A pair of scaffolds was prepared for each miniature pig — one for each side of the mandible. Loading procedures were conducted on a laboratory bench (Fig. 1D). The first scaffold was loaded with 100 $μg/cm^3$ of *rh*BMP-2 (recombinant human bone morphogenetic protein-2; Creative BioMart, Shirley, NY, USA)), derived from *E. coli*, and was embedded within a collagen hydrogel (4 mg/mL collagen; RatCol® Rat Tail Collagen for 3D Hydrogels; Advanced Biomatrix, San Diego, CA, USA). In contrast, the second scaffold was loaded solely with a collagen hydrogel, serving as the control group. The collagen hydrogel was prepared according to the manufacturer's instructions.

2.4. Surgical procedure

All implantation procedures were conducted by a team of

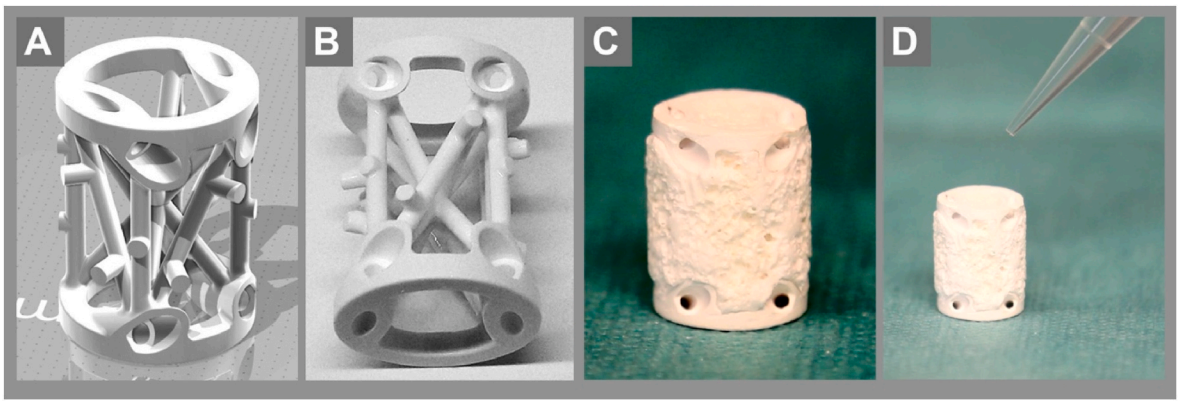

Fig. 1. (A) CAD-developed support structure. (B) CerAM VPP manufactured support structure fabricated from ZrO_2-TCP. (C) Freeze foam-filled and sintered hybrid scaffold. (D) Pre-surgical *rh*BMP-2/hydrogel loading.

experienced surgeons following standardized protocols. The process commenced with the administration of sedation through intraperitoneal injection of 2 mg/kg bodyweight xylazine 2%, 20 mg/kg body weight ketamine 10%, and 0.04 mg/kg bw atropine sulfate (0.05 mg/mL). Propofol (1 mg/kg body weight) was delivered through a vena auricularis indwelling catheter, followed by endotracheal intubation. Anesthesia was then maintained by inhalation of isoflurane 1–2 vol%. Mechanical ventilation was performed using 50% oxygen, while fluid loss during anesthesia was counterbalanced by infusing 10 mL/kg body weight/h of Ringer's solution. Additionally, 5 mL of articaine (4% with epinephrine 1:100 000) was preoperatively injected into the surgical site for local anesthesia, and the animals received 50 mg/kg body weight metamizole and 0.4 mg/kg bodyweight meloxiam for analgesia during surgery.

Animals were fixed in a dorsal/supine position and an aseptic operation was prepared (Fig. 2A). After cutting through the neck fascia and detaching the periosteum, the bone defect size for the cylindrical scaffold was marked above the base of the mandible using a template (Fig. 2B). The preparation of the bone defect was carried out using a piezo osteotome and a Lindemann milling machine (Fig. 2B and C). The scaffolds were placed (Fig. 2D) and fixed to the surrounding bone with sutures (Fig. 2E). Ultimately, a multi-layer closure technique was employed to seal the access wound, encompassing layers such as the periosteum, neck fascia, subcutaneous tissue, and skin (Fig. 2F). Suture removal took place during subsequent sedations scheduled for the fluorochrome injections. To ensure proper postoperative care, amoxicillin was administered intraoperatively for antibiotic therapy, followed by a 5-day regimen involving two daily doses of 20 mg amoxicillin per kilogram of body weight.

2.5. Computed tomography

Each of the ten animals underwent computed tomography (CT) examinations at the 4-, 8-, and 12-week marks following implantation (Fig. 3). The examination was performed by an experienced radiographer and the analysis of the images by an experienced radiologist. The radiologist drew regions of interest (ROIs) within the scaffolds on the derived CT images by including multiple ROIs on different parts of the scaffolds. From these ROIs, the mean density values for each scaffold in Hounsfield units (HU) were extracted. A 64-slice CT scanner (Somatom

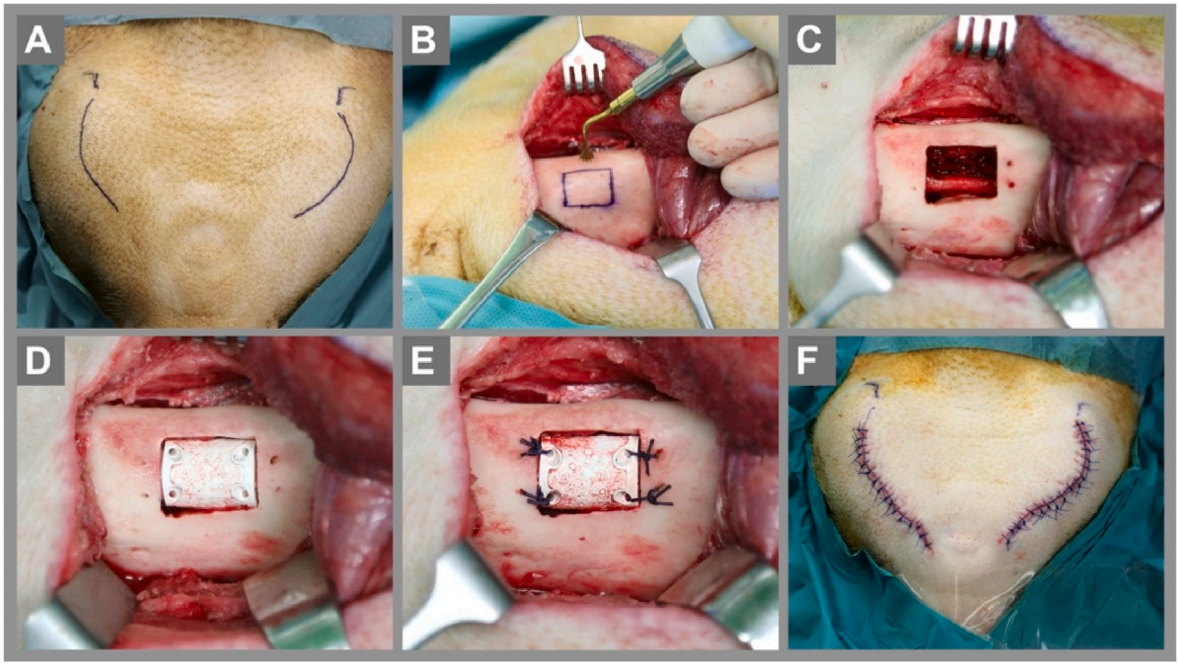

Fig. 2. Surgical procedure. (A) Marking of the jaw angle and the bilateral incision. (B) Creation of the mandibular bone defect using a piezotome. (C) The course of the inferior alveolar nerve can be seen within the defect. (D) Scaffold inserted into the defect. (E) Fixed scaffold. (F) Postoperative situation.

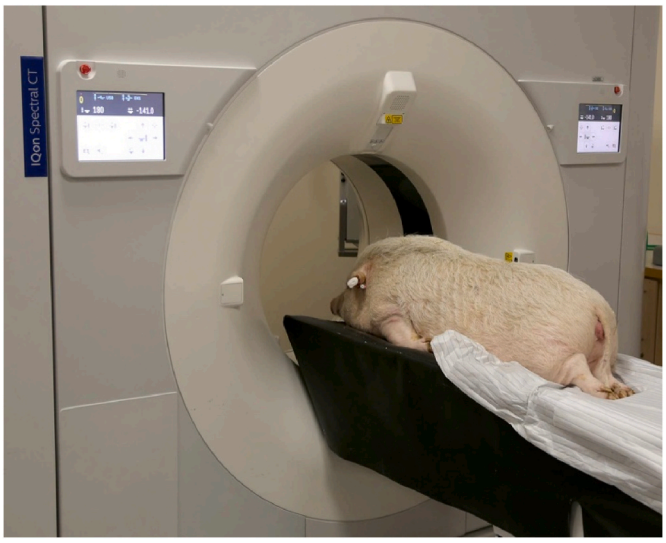

Fig. 3. All minipigs underwent CT examination at 4, 8, and 12 weeks post-implantation.

Sensation 64, Siemens Healthineers) was used for imaging. CT images were acquired using a slice thickness of 1 mm. The images were analyzed using our institutional Picture Archiving and Communication System (PACS).

2.6. Fluorochrome sequence labeling

Fluorochrome markers were administered through intraperitoneal injections every 2 weeks following the surgical procedure, using peripheral venous access (Table 1). These injections were performed while the animals were under neuroleptanalgesia, with intraperitoneal injection under neuroleptanalgesia (injection of 2 mg/kg body weight xylazine 2%, 20 mg/kg body weight ketamine 10%, and 0.04 mg/kg bw atropine sulfate).

2.7. Examination of bone regeneration

After 3 months, the animals were euthanised under deep anesthesia through an intravenous injection of 7.45% potassium chloride (220 mg/kg of body weight). Following confirmation of death, the implants and surrounding tissue were harvested and preserved in 4% formalin.

Initially, the scaffolds underwent microtomography (μCT) scanning using a SCANCO VivaCT-80 system from SCANCO Medical AG in Brüttisellen, Switzerland. This process occurred at the Molecular Imaging North Competence Center (MOIN-CC) in Kiel. The X-ray parameters for acquiring the 3D images were set to 70 kVp, 114 μA, and 8 W, and a Cu 0.1 mm filter was employed. The resulting voxel size was 24.2 μm, with 867 slices being scanned.

Table 1
Intravital fluorochrome labeling.

Fluorochrome	Colour	Dose	Time of labeling after implantation
Xylenol orange	Orange	6% in 2% $NaHCO_3$-solution, 90 mg/kg body weight	2 weeks
Calcein-green	Green	1% in 2% $NaHCO_3$-solution, 15 mg/kg body weight	4 weeks
Alizarin complexone	Red	2% in 2% $NaHCO_3$-solution, 30 mg/kg body weight	6 weeks
Tetracyclin	Brown	3% in 2% $NaHCO_3$-solution, 30 mg/kg body weight	8 weeks
Calcein-green	Green	1% in 2% $NaHCO_3$-solution, 15 mg/kg body weight	10 weeks

[a] $NaHCO_3$-solution: Sigma-Aldrich, Steinheim, Germany.

Quantitative analysis of the acquired μCT data was conducted utilizing two software tools: uct_evaluate from SCANCO Medical AG in Brüttisellen, Switzerland, and StructuralInsight (version 3.1.4) from the Biomedical Imaging section of MOIN-CC.

Non-implanted hybrid scaffolds were employed as empty controls in the study. The radiological density assessment of the scaffolds took place across three distinct regions: the central ring (with a radius of 3 mm), the first ring (spanning from 3 mm to 4.5 mm radius), and a second ring (encompassing 4.5–6 mm radius). Within each group, the calculated mean values (in mg hydroxyapatite/cm^3), along with their corresponding standard deviations, were determined based on all recorded density measurements.

Next, the specimens underwent processing for histological analysis. The scaffolds were precisely sectioned at their center using a diamond-coated saw, resulting in three non-decalcified slices of 40 μm thickness for each scaffold. The evaluation commenced with fluorescence microscopy, utilizing the Axio Observer.Z1 system and Axio Cam, with Axio Vision software, all from Carl Zeiss Mikroskopie in Jena, Germany. Subsequently, a toluidine-blue staining procedure was conducted, followed by examination under light microscopy. Detailed photographs of the scaffold slices were captured, and histomorphometric analysis was performed using Axio Cam and Axio Vision Standard through the Axio Observer.Z1 setup from Carl Zeiss Mikroskopie.

The assessment encompassed several aspects, including the area proportion of newly formed bone, the remaining TCP foam, and the direct contact region between autologous bone and the supporting struts of the scaffolds. Adjacent soft-tissue samples were embedded in paraffin, yielding 6 μm-thick sections stained using hematoxylin-eosin. For the histological evaluation, quantities of distinct granulocyte types, foreign body cells (giant cells), lymphocytes, fibrotic tissue, and capillary ingrowths were quantified across ten fields of view, all observed under 100 × magnification.

2.8. Statistics

The mean value and corresponding standard deviation were calculated for all recorded measurements. A two-sided *t*-test was conducted, with a significance level of $p < 0.05$. For semiquantitative analysis, the median was determined.

3. Results

3.1. General findings

All animals were successfully rehabilitated after surgery. They could consume regular food starting on the first day postsurgery, and their body weight remained consistent. The wounds healed primarily without complications, and there were no indications of local or systemic side effects.

3.2. Computed tomography

All ten minipigs underwent CT examinations at 4, 8, and 12 weeks post-implantation. The average radiological density of the scaffolds was measured after 4 weeks, yielding a value of 2513 ± 128 HU in the *rh*BMP-2 group and 2430 ± 131 HU in the group without *rh*BMP-2. At the 8-week mark, the densities were recorded as 2474 ± 153 HU in the *rh*BMP-2 group and 2584 ± 119 HU in the control group. After 12 weeks, a slight density increase was observed, measuring 2606 ± 115 HU in the *rh*BMP-2 group and 2601 ± 67 HU in the non-*rh*BMP-2 group.

A progressive superstructural reaction, characterized by an

increasing density of the foreign material in question, was evident across all samples. An initial periosteal reaction, indicative of mild inflammation, was observed in four animals (comprising eight scaffolds). This reaction exhibited regression over 12 weeks. Notably, CT examinations did not reveal any heterotopic ossifications (Fig. 4).

3.3. Microtomography (μCT)

Scaffold density was assessed by analyzing post-mortem μCT scans (Fig. 5). The calculated scaffold densities amounted to 1346 ± 71 mg hydroxyapatite/cm^3 in the *rh*BMP-2 group and 1282 ± 91 mg hydroxyapatite/cm^3 in the control group ($p = 0.045$). The density of identically constructed samples, scanned prior to implantation, was measured at 1508 ± 30 mg hydroxyapatite/cm^3.

3.4. Histology findings

Fluorescence microscopy revealed evident bone growth within the foam structure, spanning the defect gap, and newly formed bone adhering to the ZrO_2-TCP support struts. The images consistently showed the presence of all labeled fluorescence markers at the designated time points of fluorescence labeling — specifically, after 2, 4, 6, 8, and 10 weeks (Fig. 6C and E). Within the foam, the distribution of fluorochromes displayed an uneven pattern, with a greater concentration of calcein-green observable in the central basal region of the scaffold. In contrast, the growth of bone within the defect gap (Fig. 7) exhibited a uniform progression over time.

Fig. 4. (A) CT scan of the miniature pig as an overview. (B) CT scan of the scaffolds in the mandible as a cross-section on the right side and in detail on the left side in yellow.

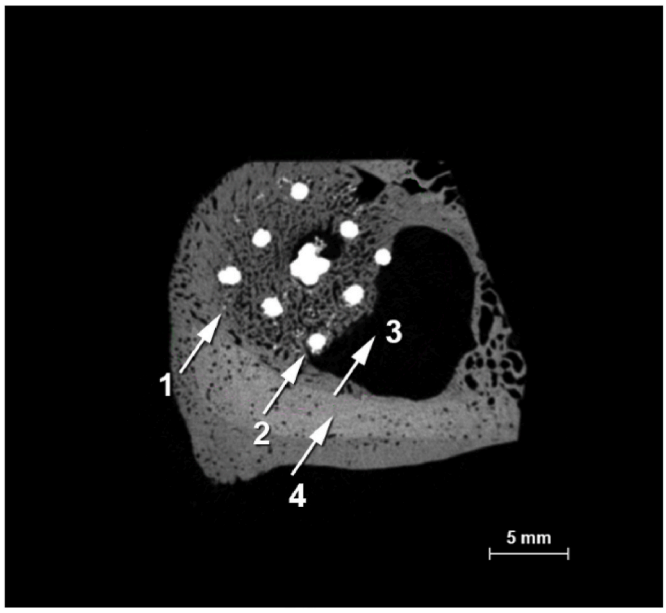

Fig. 5. Radiographic image of the scaffold in the μCT scan: (Wang et al., 2011) ossification in the defect gap; (Feuvrier et al., 2016) non-degraded scaffold support struts; (Zimmermann et al., 2001) nerve canal; and (Berzofsky et al., 2013) surrounding bone.

Microscopy images of toluidine-blue-stained samples vividly showed autologous bone growth within the TCP foam scaffold and the defect gap across both experimental groups (Fig. 6A, B, and D). Quantitatively, the area proportion of newly formed bone reached 48 ± 10% within the *rh*BMP-2 group, marking a significant increase compared with the group without *rh*BMP-2 (42 ± 9%; $p = 0.03$). Furthermore, the average area proportion of the residual TCP foam was measured at 23 ± 8% for the *rh*BMP-2 group, compared with 24 ± 10% for the non-*rh*BMP-2 group. It is worth noting that the measured TCP foam area proportion for the control scaffolds before implantation was 46 ± 2%. Consequently, during the 3-month trial period, 50% (in the *rh*BMP-2 group) and 48% (in the non-*rh*BMP-2 group) of the TCP material experienced degradation.

The proportion of bone attached to the ZrO_2-TCP-supporting struts was measured at 51 ± 22% (*rh*BMP-2 group) and 61 ± 16% (control group). A semi-quantitative evaluation showed that complete bone growth had occurred within the defect gap in both experimental groups (Table 2).

Furthermore, it was evident that in nine out of ten scaffolds with *rh*BMP-2, the support struts at the lateral aspect were encompassed by bone tissue that was induced within the original contour of the scaffold, even if the scaffold expanded the bony defect (Fig. 8A). Conversely, in the group without *rh*BMP-2, seven of ten scaffolds exhibited peripheral degradation of the TCP-foam, resulting in soft-tissue encapsulation of the bioinert struts that expanded the bony envelope of the mandibular bone (junction line of the edges of the defect) (Fig. 8B).

Histological assessment of the adjacent soft tissues was conducted using hematoxylin-eosin staining to evaluate the presence of granulocytes, giant cells (foreign body cells), lymphocytes, fibrotic tissue, and capillary ingrowth. In ten fields of view, an average count of 0.3 granulocytes, 0.3 giant cells, and 0.3 lymphocytes was observed in the *rh*BMP-2 group. Conversely, the group without *rh*BMP-2 exhibited an average count of 0.9 granulocytes, 1.0 giant cells, and 0.7 lymphocytes. The semiquantitative assessment of capillary ingrowth and fibrosis yielded consistently unremarkable results, indicating the absence of chronic inflammation in all samples (Fig. 9).

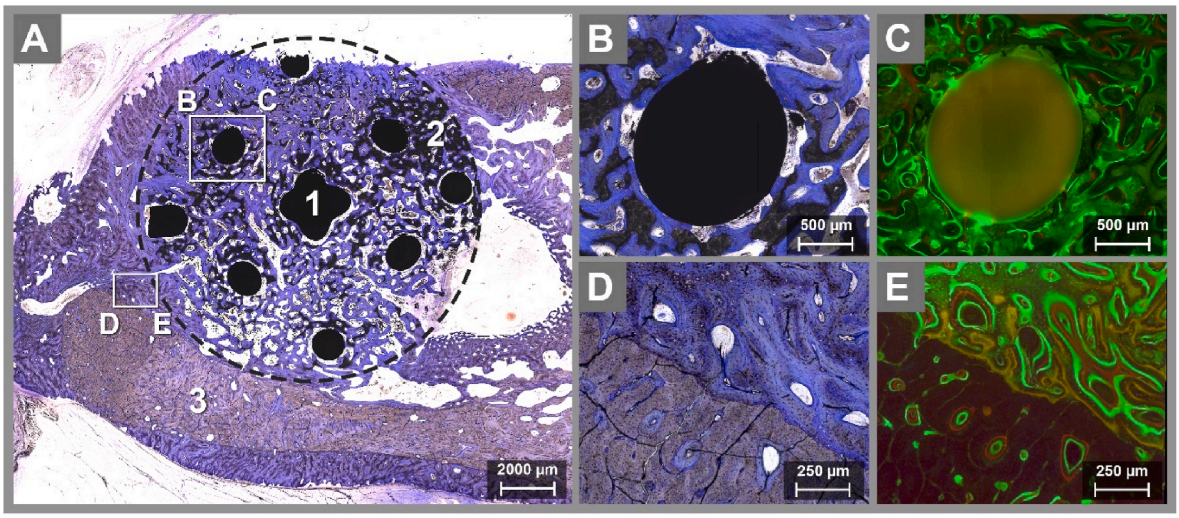

Fig. 6. Toluidine-blue staining of the scaffold shows the newly formed bone (blue). (A) Overview of the scaffold (dotted circle) and the surrounding local bone: (Wang et al., 2011) support struts (black); (Feuvrier et al., 2016) non-degraded and remaining TCP foam (dark grey); (Zimmermann et al., 2001) local bone. (B) Osseointegration of the ceramic scaffold support structure. (C) Fluorescence microscopy image demonstrating time-dependent osteointegration of the scaffold support struts. (D) Osteogenesis in the defect gap and on the local bone. (E) Fluorescence microscopy image demonstrating time-dependent bone growth within the defect gap.

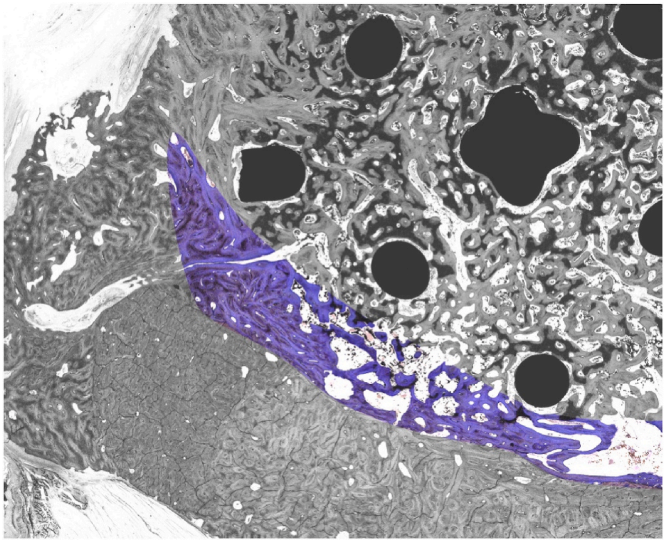

Fig. 7. Detail of the toluidine-blue stained sample, showing bone growth in the defect gap (colour-stained area).

Table 2
Semi-quantitative evaluation of bone formation in the defect gap.

Rating	Group	
	With *rh*BMP-2	Without *rh*BMP-2
− −, strong soft-tissue ingrowth	0	0
−, moderate soft-tissue ingrowth	0	1
0, weak bone growth	0	1
+, moderate bone growth	12	3
+ +, complete bone growth	18	25
Median	+ +	+ +

4. Discussion

Our study demonstrated that effective bone regeneration can be attained by implanting ZrO_2-TCP hybrid scaffolds into critical-size defects of the Göttingen minipig mandible. Incorporating *rh*BMP-2 led to enhanced bone regeneration and uniform dispersion of newly formed bone within the hybrid scaffolds.

Hydroxyapatite and TCP are well-documented in the literature as osteoconductive materials with porosity comparable to human bone (Açil et al., 2000; Warnke et al., 2004). However, due to the lack of osteoinductive properties in TCP, *rh*BMP-2, an extensively researched factor, was introduced for the stimulation of bone regeneration. BMPs are recognized for their ability to foster the proliferation and differentiation of osteoblasts (Sampath et al., 1992; Yamashita et al., 1996). Notably, there have been instances where the application of BMPs has led to heightened osteoinduction, even in muscular tissues (Katagiri et al., 1997; Yoshida et al., 1998). This elevated osteoinduction in muscle tissue is attributed to immature cells and myoblasts, which can differentiate into osteoblasts upon BMP stimulation (Bosch et al., 2000; Levy et al., 2001).

Furthermore, implanting bone substitute material is known to induce a localized inflammatory reaction, consequently promoting neovascularisation (Inoda et al., 2007). This process leads to the expression of multipotent cells through neoangiogenesis, allowing them to differentiate into bone-forming cells (Yamaguchi et al., 1996; Katagiri et al., 1994).

Our study illustrated improved and more uniform bone regeneration attributed to *rh*BMP-2-loading. However, the loading potential of other growth hormones must also be evaluated in future studies (Sachse et al., 2023).

An alternative approach to harnessing the beneficial impacts of *rh*BMP-2 involves the autonomous loading or coating of scaffolds, separate from the procedural steps. For instance, this could occur during or upon the conclusion of the manufacturing process (Hasenbein et al., 2022). However, it was decided not to use this method due to the uncertain retention of active *rh*BMP-2 at the defect site after the considerable time lapse until the surgical procedure. Moreover, the effectiveness of such coating and its timing in terms of insertion is intricately contingent and challenging to assess.

Regarding the composition of the scaffolds themselves, a variety of materials can be considered. Among these, materials with exceptional stability, such as titanium, stand out. However, as previously demonstrated by our research group, a concern arises regarding stress shielding, which can trigger bone resorption due to the absence of appropriate biomechanical stress following Wolff's law (Naujokat et al., 2018; Wiltfang et al., 2016).

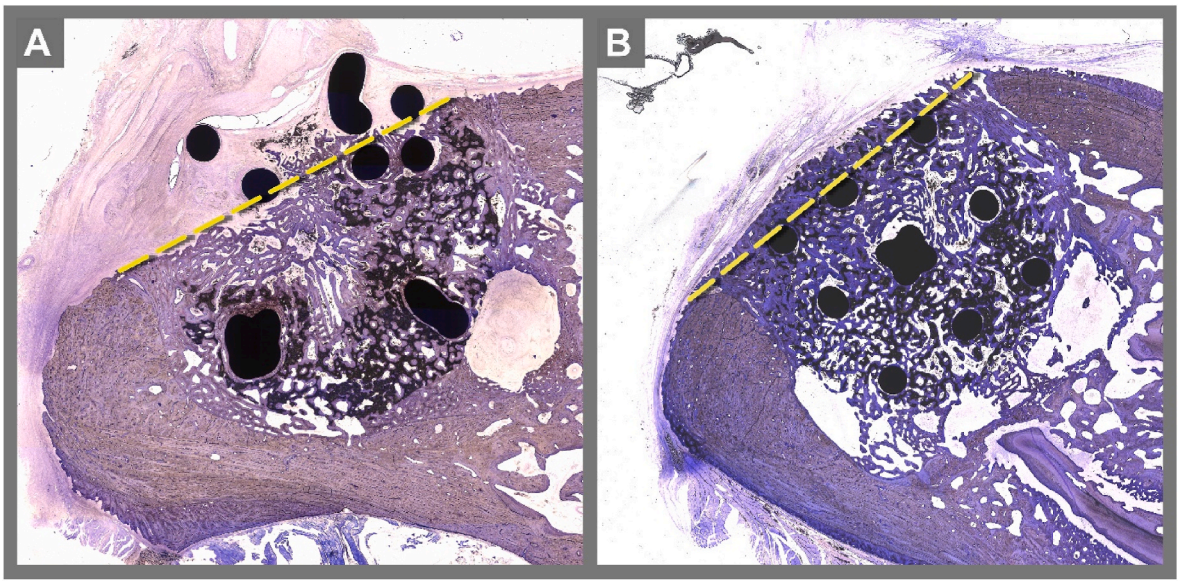

Fig. 8. (A) Scaffold without *rh*BMP-2. (B) Scaffold with *rh*BMP-2. The yellow line indicates the junction line of the local bone.

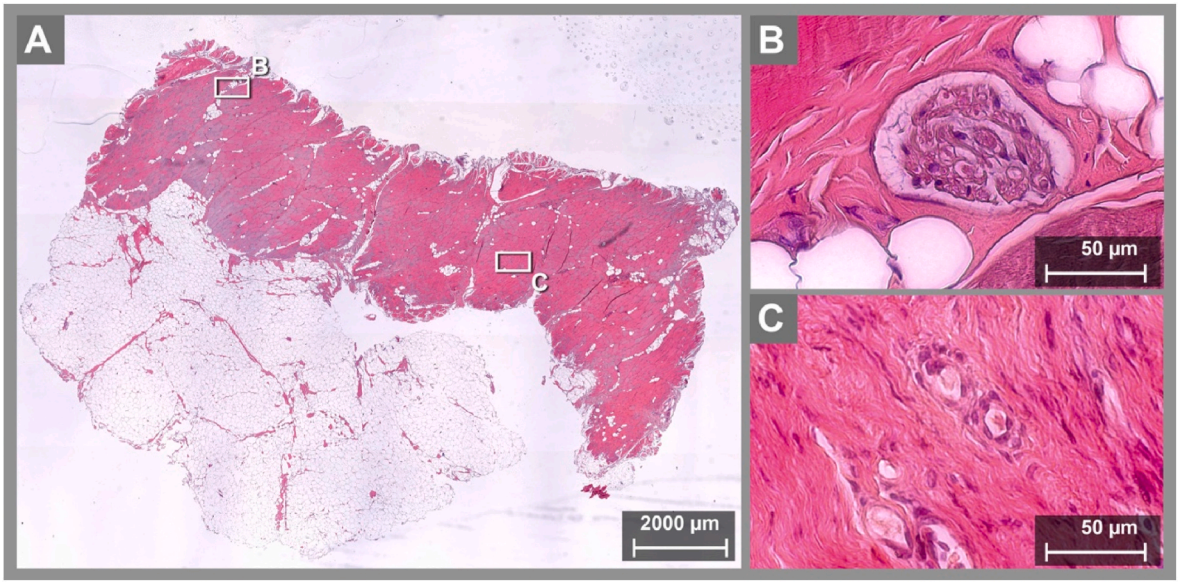

Fig. 9. (A) Overview of a soft-tissue sample of the BMP-group, consisting of longitudinal and striated muscle as well as fatty tissue. (B) Exemplary presentation of a giant cell. (C) Granulocytes.

Synthetic materials also present an option; however, these often lack the requisite mechanical stability. Consequently, they cannot yet be adopted as the standard solution for critical defects (Fernandez de Grado et al., 2018; Hannink and Arts, 2011).

The intended macrostructure conforms to the defect and ensures mechanical stability. Furthermore, the microstructure closely resembles bone marrow, facilitating cellular attachment, promoting the synthesis of the bone extracellular matrix, and enabling tissue vascularization. Thankfully, all these requisites have been successfully addressed using our ZrO_2-TCP hybrid scaffolds.

Certain limitations must be acknowledged in this study. The first pertains to the surgical procedure itself. Despite the prior implementation of digital planning and corresponding ex-vivo preliminary assessments, an intraoperative challenge emerged. The material's brittleness hindered the intended fixation of the scaffolds using bone screws. Consequently, adequate fixation was accomplished through the use of sutures. Despite this adaptation, it is important to note that minimal movements of individual scaffolds within the bone defects, possibly caused by the chewing motions of the animals during feeding, cannot be entirely ruled out. However, the absence of any indications of flawed osseointegration or inflammatory markers, both clinically and during trial procedures, as well as during the harvesting and subsequent evaluation phases, is noteworthy. Refinement of the screw-hole design is an area for improvement in future investigations.

Second, it is important to consider the dimensions of the 12×14 mm defect. This defect was introduced in the basal mandible, primarily affecting the cortical bone. Given that this region plays a critical role in mandibular stability, it is important to note that this was not a segmental defect and did not involve the tooth-bearing section. Moving forward, exploration of larger defects, including segmental ones, is imperative to thoroughly assess the scaffold's efficacy in these contexts. Moreover, the evaluation of defects within the tooth-bearing area will be important. Even with subsequent plastic coverage, a certain connection to the oral cavity persists, potentially allowing the ingress of bacteria into the

defect region and, consequently, the scaffold area. This dynamic mirrors the clinical scenario and necessitates further investigation before advancing to clinical trials.

Looking ahead, the integration of 3D planning and 3D manufacturing processes holds the potential to facilitate preoperative resection planning and tailored scaffold design spanning various anatomical regions. Furthermore, it is worth noting that the application is not confined to the maxillofacial region alone; it can also be extended to diverse anatomical domains (Sachse et al., 2023).

5. Conclusion

Effective bone regeneration can be accomplished by implanting the presented hybrid scaffolds, consisting of load-bearing ZrO_2-TCP support struts for mechanical stabilization (Ahlhelm et al., 2021) and TCP freeze foams for cell ingrowth and new bone formation, into critical-size mandibular defects in Göttingen minipigs, particularly when these scaffolds are supplemented with *rh*BMP-2. As such, the novel hybrid bone graft substitutes exhibit promising prospects for tolerability and suitability in addressing surgical interventions for critical-size defects within the maxillofacial domain.

Conflicts of interest

The authors have no conflicts of interest to declare.

Funding

This research was funded by the German Federal Ministry of Education and Research (HybridBone, grant number 03VP07631).

Ethical approval

The study protocol was approved by the Ministerium für Energiewende, Landwirtschaft, Umwelt, Natur und Digitalisierung Schleswig-Holstein (approval no. V242-75139/2020 (100-11/20)).

Patient consent

Not required.

Authorships

All authors contributed substantially to this work and have reviewed and agreed to the submission.

Declaration of competing interest

The authors have no competing interests to declare.

Acknowledgments

The authors would like to thank Gaby Neβenius and Andreas Reinhardt for their technical expertise and support in this project. They would also like to thank Timo Damm and Claus-Christian Glüer from MOIN-CC, Eileen Küchler from the Department of Radiology at UKSH Kiel, and the Department of Animal Protection and Husbandry faculty of the University of Kiel.

References

Açil, Y., Terheyden, H., Dunsche, A., Fleiner, B., Jepsen, S., 2000. Three-dimensional cultivation of human osteoblast-like cells on highly porous natural bone mineral. J. Biomed. Mater. Res. 51 (4), 703–710.

Ahlhelm, M., Günther, P., Scheithauer, U., Schwarzer, E., Günther, A., Slawik, T., et al., 2016. Innovative and novel manufacturing methods of ceramics and metal-ceramic composites for biomedical applications. J. Eur. Ceram. Soc. 36 (12), 2883–2888.

Ahlhelm, M., Schwarzer, E., Scheithauer, U., Moritz, T., Michaelis, A., 2017. Novel ceramic composites for personalized 3D structures. J. Ceram. Sci. Technol. 8, 91–100.

Ahlhelm, M., Latorre, S.H., Mayr, H.O., Storch, C., Freytag, C., Werner, D., et al., 2021. Mechanically stable β-TCP structural hybrid scaffolds for potential bone replacement. Journal of Composites Science 5 (10), 281.

Becker, S.T., Bolte, H., Krapf, O., Seitz, H., Douglas, T., Sivananthan, S., et al., 2009. Endocultivation: 3D printed customized porous scaffolds for heterotopic bone induction. Oral Oncol. 45 (11), e181–e188.

Berzofsky, C., Shin, E., Mashkevich, G., 2013. Leg compartment syndrome after fibula free flap. Otolaryngol. Head Neck Surg. 148 (1), 172–173.

Bosch, P., Musgrave, D.S., Lee, J.Y., Cummins, J., Shuler, T., Ghivizzani, T.C., et al., 2000. Osteoprogenitor cells within skeletal muscle. J. Orthop. Res. 18 (6), 933–944.

Fernandez de Grado, G., Keller, L., Idoux-Gillet, Y., Wagner, Q., Musset, A.M., Benkirane-Jessel, N., et al., 2018. Bone substitutes: a review of their characteristics, clinical use, and perspectives for large bone defects management. J. Tissue Eng. 9, 2041731418776819.

Feuvrier, D., Sagawa Jr., Y., Béliard, S., Pauchot, J., Decavel, P., 2016. Long-term donor-site morbidity after vascularized free fibula flap harvesting: clinical and gait analysis. J. Plast. Reconstr. Aesthetic Surg. 69 (2), 262–269.

Ganry, L., Quilichini, J., Bandini, C.M., Leyder, P., Hersant, B., Meningaud, J.P., 2017. Three-dimensional surgical modelling with an open-source software protocol: study of precision and reproducibility in mandibular reconstruction with the fibula free flap. Int. J. Oral Maxillofac. Surg. 46 (8), 946–957.

Gruskin, E., Doll, B.A., Futrell, F.W., Schmitz, J.P., Hollinger, J.O., 2012. Demineralized bone matrix in bone repair: history and use. Adv. Drug Deliv. Rev. 64 (12), 1063–1077.

Hannink, G., Arts, J.J., 2011. Bioresorbability, porosity and mechanical strength of bone substitutes: what is optimal for bone regeneration? Injury 42 (Suppl. 2). S22–5.

Hasenbein, I., Sachse, A., Hortschansky, P., Schmuck, K.D., Horbert, V., Anders, C., et al., 2022. Single application of low-dose, hydroxyapatite-bound BMP-2 or GDF-5 induces long-term bone formation and biomechanical stabilization of a bone defect in a senile sheep lumbar osteopenia model. Biomedicines 10 (2).

Inoda, H., Yamamoto, G., Hattori, T., 2007. rh-BMP2-induced ectopic bone for grafting critical size defects: a preliminary histological evaluation in rat calvariae. Int. J. Oral Maxillofac. Surg. 36 (1), 39–44.

Jo, Y.Y., Kim, S.G., Kim, M.K., Shin, S.H., Ahn, J., Seok, H., 2018. Mandibular reconstruction using a customized three-dimensional titanium implant applied on the lingual surface of the mandible. J. Craniofac. Surg. 29 (2), 415–419.

Katagiri, T., Yamaguchi, A., Komaki, M., Abe, E., Takahashi, N., Ikeda, T., et al., 1994. Bone morphogenetic protein-2 converts the differentiation pathway of C2C12 myoblasts into the osteoblast lineage. J. Cell Biol. 127 (6 Pt 1), 1755–1766.

Katagiri, T., Akiyama, S., Namiki, M., Komaki, M., Yamaguchi, A., Rosen, V., et al., 1997. Bone morphogenetic protein-2 inhibits terminal differentiation of myogenic cells by suppressing the transcriptional activity of MyoD and myogenin. Exp. Cell Res. 230 (2), 342–351.

Khorasani, M., Janbaz, P., Rayati, F., 2018. Maxillofacial reconstruction with Medpor porous polyethylene implant: a case series study. J Korean Assoc Oral Maxillofac Surg 44 (3), 128–135.

Kirker-Head, C.A., 2000. Potential applications and delivery strategies for bone morphogenetic proteins. Adv. Drug Deliv. Rev. 43 (1), 65–92.

Levy, M.M., Joyner, C.J., Virdi, A.S., Reed, A., Triffitt, J.T., Simpson, A.H., et al., 2001. Osteoprogenitor cells of mature human skeletal muscle tissue: an in vitro study. Bone 29 (4), 317–322.

Miron, R.J., Zhang, Y.F., 2012. Osteoinduction: a review of old concepts with new standards. J. Dent. Res. 91 (8), 736–744.

Moore, W.R., Graves, S.E., Bain, G.I., 2001. Synthetic bone graft substitutes. ANZ J. Surg. 71 (6), 354–361.

Naujokat, H., Açil, Y., Gülses, A., Birkenfeld, F., Wiltfang, J., 2018. Man as a living bioreactor: long-term histological aspects of a mandibular replacement engineered in the patient's own body. Int. J. Oral Maxillofac. Surg. 47 (11), 1481–1487.

Patel, K., Brandstetter, K., 2016. Solid implants in facial plastic surgery: potential complications and how to prevent them. Facial Plast. Surg. 32 (5), 520–531.

Rana, M., 2017. Three-dimensional planning and computer-assisted surgery in craniofacial reconstruction. Int. J. Oral Maxillofac. Surg. 46, 44.

Rana, M., Chin, S.J., Muecke, T., Kesting, M., Groebe, A., Riecke, B., et al., 2017. Increasing the accuracy of mandibular reconstruction with free fibula flaps using functionalized selective laser-melted patient-specific implants: a retrospective multicenter analysis. J. Cranio-Maxillo-Fac. Surg. 45 (8), 1212–1219.

Ritschl, L.M., Mücke, T., Fichter, A., Güll, F.D., Schmid, C., Duc, J.M.P., et al., 2017. Functional outcome of CAD/CAM-assisted versus conventional microvascular, fibular free flap reconstruction of the mandible: a retrospective study of 30 cases. J. Reconstr. Microsurg. 33 (4), 281–291.

Sachse, A., Hasenbein, I., Hortschansky, P., Schmuck, K.D., Maenz, S., Illerhaus, B., et al., 2023. BMP-2 (and partially GDF-5) coating significantly accelerates and augments bone formation close to hydroxyapatite/tricalcium-phosphate/brushite implant cylinders for tibial bone defects in senile, osteopenic sheep. J. Mater. Sci. Mater. Med. 34 (7), 31.

Sadr-Eshkevari, P., Rashad, A., Vahdati, S.A., Garajei, A., Bohluli, B., Maurer, P., 2013. Alloplastic mandibular reconstruction: a systematic review and meta-analysis of the current century case series. Plast. Reconstr. Surg. 132 (3), 413e–27e.

Sampath, T.K., Maliakal, J.C., Hauschka, P.V., Jones, W.K., Sasak, H., Tucker, R.F., et al., 1992. Recombinant human osteogenic protein-1 (hOP-1) induces new bone formation in vivo with a specific activity comparable with natural bovine osteogenic protein and stimulates osteoblast proliferation and differentiation in vitro. J. Biol. Chem. 267 (28), 20352–20362.

Wang, E.A., Rosen, V., Cordes, P., Hewick, R.M., Kriz, M.J., Luxenberg, D.P., et al., 1988. Purification and characterization of other distinct bone-inducing factors. Proc. Natl. Acad. Sci. U. S. A. 85 (24), 9484–9488.

Wang, K.H., Inman, J.C., Hayden, R.E., 2011. Modern concepts in mandibular reconstruction in oral and oropharyngeal cancer. Curr. Opin. Otolaryngol. Head Neck Surg. 19 (2), 119–124.

Warnke, P.H., Springer, I.N., Wiltfang, J., Acil, Y., Eufinger, H., Wehmöller, M., et al., 2004. Growth and transplantation of a custom vascularised bone graft in a man. Lancet 364 (9436), 766–770.

Wiltfang, J., Rohnen, M., Egberts, J.H., Lützen, U., Wieker, H., Açil, Y., et al., 2016. Man as a living bioreactor: prefabrication of a custom vascularized bone graft in the gastrocolic omentum. Tissue Eng. C Methods 22 (8), 740–746.

Wozney, J.M., Rosen, V., Celeste, A.J., Mitsock, L.M., Whitters, M.J., Kriz, R.W., et al., 1988. Novel regulators of bone formation: molecular clones and activities. Science 242 (4885), 1528–1534.

Yamada, M., Egusa, H., 2018. Current bone substitutes for implant dentistry. J Prosthodont Res 62 (2), 152–161.

Yamaguchi, A., Ishizuya, T., Kintou, N., Wada, Y., Katagiri, T., Wozney, J.M., et al., 1996. Effects of BMP-2, BMP-4, and BMP-6 on osteoblastic differentiation of bone marrow-derived stromal cell lines, ST2 and MC3T3-G2/PA6. Biochem. Biophys. Res. Commun. 220 (2), 366–371.

Yamashita, H., Ten Dijke, P., Heldin, C.H., Miyazono, K., 1996. Bone morphogenetic protein receptors. Bone 19 (6), 569–574.

Yoshida, K., Bessho, K., Fujimura, K., Kusumoto, K., Ogawa, Y., Tani, Y., et al., 1998. Osteoinduction capability of recombinant human bone morphogenetic protein-2 in intramuscular and subcutaneous sites: an experimental study. J. Cranio-Maxillo-Fac. Surg. 26 (2), 112–115.

Zimmermann, C.E., Börner, B.I., Hasse, A., Sieg, P., 2001. Donor site morbidity after microvascular fibula transfer. Clin. Oral Invest. 5 (4), 214–219.